Constraining the source of mantle plumes

N. Cagney[a], F. Crameri[a], W. H. Newsome[b], C. Lithgow-Bertelloni[a], A. Cotel[c], S. R. Hart[d], J. A. Whitehead[e]

[a]*Department of Earth Sciences, University College London, Gower Street, London, WC1E 6BT, UK.*
[b]*Department of Geological Sciences, University of Michigan, Ann Arbor, Michigan, USA.*
[c]*Department of Civil and Environmental Engineering, University of Michigan, Ann Arbor, Michigan, USA.*
[d]*Geology and Geophysics Department, Woods Hole Oceanographic Institute, Woods Hole, Massachusetts, USA.*
[e]*Physical Oceanography Department, Woods Hole Oceanographic Institute, Woods Hole, Massachusetts, USA.*

Abstract

In order to link the geochemical signature of hot spot basalts to Earth's deep interior, it is first necessary to understand how plumes sample different regions of the mantle. Here, we investigate the relative amounts of deep and shallow mantle material that are entrained by an ascending plume and constrain its source region. The plumes are generated in a viscous syrup using an isolated heater for a range of Rayleigh numbers. The velocity fields are measured using stereoscopic Particle-Image Velocimetry, and the concept of the 'vortex ring bubble' is used to provide an objective definition of the plume geometry. Using this plume geometry, the plume composition can be analysed in terms of the proportion of material that has been entrained from different depths. We show that the plume composition can be well described using a simple empirical relationship, which depends only on a

Email address: neil.cagney.11@ucl.ac.uk (N. Cagney)

single parameter, the sampling coefficient, s_c. High-s_c plumes are composed of material which originated from very deep in the fluid domain, while low-s_c plumes contain material entrained from a range of depths. The analysis is also used to show that the geometry of the plume can be described using a similarity solution, in agreement with previous studies. Finally, numerical simulations are used to vary both the Rayleigh number and viscosity contrast independently. The simulations allow us to predict the value of the sampling coefficient for mantle plumes; we find that as a plume reaches the lithosphere, 90% of its composition has been derived from the lowermost $260-750$ km in the mantle, and negligible amounts are derived from the shallow half of the lower mantle. This result implies that isotope geochemistry cannot provide direct information about this un-sampled region, and that the various known geochemical reservoirs must lie in the deepest few hundred kilometres of the mantle.
Keywords:

---

1. Introduction

Heat flow from radiogenic elements and the cooling of the core causes the mantle to undergo continuous convection. One consequence of this is the appearance of plumes; columns of hot, buoyant material which rise through the mantle, causing intraplate volcanism at several hotspots. The formation of Large Igneous Provinces (LIPs) is generally attributed to the initial arrival of plumes at the lithosphere, while ocean island chains are thought to arise from the interaction between the remaining plume and the over-riding plate (Campbell, 2005; Morgan, 1971; Richards et al., 1989).

The basalts formed at these ocean islands (OIBs) tend to be highly heterogeneous, relative to those formed at spreading centres, and there is considerable variation between the chemical signatures of OIBs found at different hot spots (Hawkesworth and Scherstén, 2007; Kellogg, 1992). This indicates that plumes are derived from a strongly heterogenous source - or have more than one distinct source (Hofmann, 1997) - but it remains unclear where these sources lie or how OIBs should be interpreted in terms of the overall chemical composition of the mantle. For example, there is disagreement over whether the heterogeneity in OIBs is indicative of the overall heterogeneity in the mantle, or whether it is simply represents the chemical state near the thermal boundary layer where the plume formed (Hofmann and Farnetani, 2013). Similarly, the high $^{3}He/^{4}He$ signatures of OIBs at some hot spots indicate the existence of reservoirs of 'primitive' material that have remained isolated from the convecting mantle for billions of years (Tackley, 2000; van Keken et al., 2002); however, it is not known where in the mantle these reservoirs lie.

The composition of a plume is determined by its entrainment process. Early flow visualisation experiments of thermal plumes by Griffiths and Campbell (1990) showed that plumes contain a large head followed by a narrower tail, and that plumes can entrain ambient material by mechanically 'stirring' it into the vortices in the plume head. However, the numerical simulations of Farnetani and Richards (1995) and experiments by Cagney et al. (2015) found that the contribution of mechanical stirring to the entrainment process was relatively insignificant when the plume was generated from an isolated heat source. Farnetani and Richards (1995) argued that

the high rates observed by Griffiths and Campbell (1990) were a result of their experimental system, which involved the injection of a buoyant fluid into a vessel of fluid with a higher viscosity, rather than the use of a heater. Hauri et al. (1994) presented a similarity solution for the steady-state structure of the plume stem, and suggested that entrainment occurs by the radial conduction of heat away from the stem.

Knowledge of how plumes entrain ambient material is crucial to understanding what effect plumes will have on the creation or removal of chemical heterogeneity in the mantle. Entrainment (or the lack thereof) has been used to explain various geological and geochemical features associated with hot spots. For example, Hart et al. (1992) and Walker et al. (1995) argued on the basis of the geochemical signature of ocean island basalts that plumes do not entrain significant amounts of material from the mid- or shallow mantle, but are derived from the region close to the core-mantle boundary. In contrast, Bianco et al. (2008) argued that the geochemical signatures of many ocean island basalts could be explained by a plume entraining heterogeneous material throughout the mantle. In spite of the importance of plumes for our understanding of the deep mantle, their composition remains largely unknown. In part this is because there is no accepted or objective means to quantify the geometry or volume of a plume, and therefore it is difficult to define what material is contained within the plume and how this may change with time.

Turner (1957) showed that plumes are a special case of vortex rings, as the vortices in the plume head form a torus in three-dimensions. The vortex ring structure is particularly clear in the flow visualisation images of

Griffiths (1986) and Griffiths and Campbell (1990). This approach was used by subsequent researchers studying plumes (e.g. Chay and Schlien (1986); Pottebaum and Gharib (2004); Schlien (1976); Shusser and Gharib (2000)). The volume of turbulent vortex rings is often identified using the concept of the 'vortex ring bubble' (VRB) (Shariff and Leonard, 1992). The VRB is defined by the streamlines which enclose the vortex ring, calculated in a reference frame moving with the vortices, as will be described in more detail in Section 3.1. This concept was used by Dabiri and Gharib (2004) to examine the rates of entrainment of vortex rings under various conditions.

This paper extends the concept of the vortex ring bubble to thermal plumes to quantify their geometry and source region. The remainder of the paper is structured as follows; the experimental system and analysis tools are described in the following section; Section 3.1 demonstrates the calculation of the VRB and compares it to various Lagrangian descriptions of the flow; the plume composition is examined in Section 3.2; the analysis is applied to numerical simulations at mantle conditions in Section 4; the implications for mantle dynamics and isotope geochemistry are discussed in Section 5; and finally some concluding remarks are made.

2. Experimental details

The experiments were performed in a sealed cubic test-section, which had internal dimensions of 265 mm and 10 mm thick walls, as shown in Figure 1. The test-section was surrounded by a thermal bath, which was held at 25.2°C. The thermal plume was generated using a circular heater in the centre of the test-section, which had a diameter of 20 mm and was installed

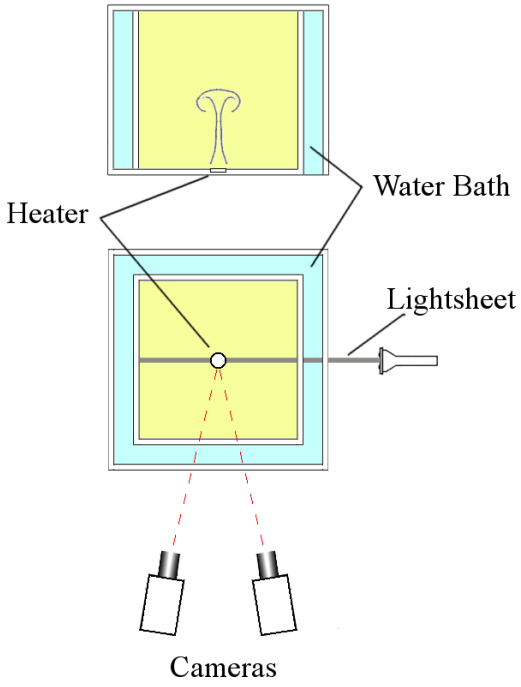

Figure 1: Elevation (top) and plan view (bottom) of the test-section and PIV system.

flush with the bottom surface. A closed-loop feedback controller was used to ensure that the heater temperature was held constant to within ± 0.25°C of the target temperature.

The working fluid was corn syrup (LSI Speciality Products' Liquidose 436), which has a Newtonian but strongly temperature-dependent viscosity. The density and viscosity were measured in the laboratory (see Cagney et al. (2015) for more details). The syrup had a density, ρ of 1439 kg/m^3 at 25.2°C and a coefficient of thermal expansion, α, of 3.1×10^{-4}°C^{-1}. The viscosity was found to vary as

$$\mu = 1080 e^{-0.156T + 6.25 \times 10^{-4} T^2} \, [\text{Pa.s}] \, , \tag{1}$$

where T is temperature in degrees Celsius. The thermal diffusivity and specific heat capacity were supplied by the manufacturer as $\kappa = 1.04 \times 10^{-7}$ m^2/s and $C_p = 2280$ J/kg.K, respectively. These values correspond to a Prandtl number of $Pr = \mu/\rho\kappa = 2.15 \times 10^5$. The numerical simulations of Whitehead et al. (2013) show that when the Prandtl number is greater than $\sim 10^3$, the dynamics of thermal plumes are essentially identical to those calculated at an infinite Prandtl number, confirming that our experiments are relevant to the mantle.

The temperature difference between the heater and the ambient fluid, ΔT, is non-dimensionalised as the Rayleigh number

$$Ra = \frac{\rho\alpha\Delta T g D^3}{\mu\kappa}, \tag{2}$$

where g is the acceleration due to gravity, and D is the depth of the fluid domain. Four experiments were performed in which ΔT was set to 24.9°C, 34.8°C, 44.9°C and 54.9°C, which corresponded to a Rayleigh number range of $(0.62 - 1.36) \times 10^6$ and a viscosity contrast range of $\gamma = \mu/\mu_{min} = 15.1 - 141.4$ (Equation 1).

The velocity fields associated with the thermal plume were measured using stereoscopic-Particle Image Velocimetry (PIV). The syrup was uniformly seeded using a high-gloss polymer powder which had a diameter in the range $1 - 40$ μm, and the measurement plane was illuminated using a halogen white light source and a fibre optic line generator. Images were acquired simultaneously using two CCD cameras, separated by 18°, as shown in Figure 1. The images from each camera were processed using a two-pass cross-correlation scheme, and the fields from the two cameras were combined to

find the three-component velocity field. Throughout each experiment, 41 velocity fields were acquired.

The final velocity fields spanned the range $x = -85.5$ mm to 78.8 mm and $y = 1.39$ mm to 215.9 mm (which is referred to as the PIV domain), where x and y are measured in the horizontal and vertical directions, respectively, with the origin fixed as the centre of the heater surface. The fields had a resolution of 2.79 mm in both directions.

The velocity fields are also analysed using a Lagrangian approach, which has been shown to be an effective means of visualising the plume structure (Farnetani et al., 2002; Lin and van Keken, 2006; Cagney et al., 2015). The Lagrangian Coherent Structures (LCSs) can be estimated using the Finite-Time Lyapunov Exponent (FTLE) (Haller, 2015), which is a measure of the maximum rate of separation of neighbouring fluid particles over the period t_0 to t. The FTLE therefore also serves as an indicator of regions of strong fluid stretching.

In order to calculate the FTLE, it is first necessary to calculate the flow map

$$\psi\left(\mathbf{x}, t, t_0\right) = \mathbf{x}\left(t, t_0, \mathbf{x_0}\right), \tag{3}$$

which describes the dynamic position of tracers in the flow that had an initial spacing $\mathbf{x_0}$ at t_0. This is found by numerically advecting passive tracers throughout the measured velocity fields using a fourth order Runge-Kutta scheme with linear interpolation in time and space. The tracers were uniformly distributed throughout the PIV domain with a spacing of 0.93 mm $\times$ 0.93 mm, i.e. three times the spatial resolution of the vector

fields.

The FTLE field is then given by

$$\sigma_f\left(\mathbf{x}, t, t_0\right) = \frac{1}{|t - t_0|} \log\left(\left|\left|\frac{\mathrm{d}\psi\left(\mathbf{x}, t, t_0\right)}{\mathrm{d}\mathbf{x_0}}\right|\right|\right), \tag{4}$$

where $||\cdot||$ represents the maximum real eigenvalue of the Cauchy-Green tensor.

The FTLE fields were computed in backward-time by reversing the flow and advecting the tracers backwards from t to $t_0 = 0$ (i.e. until the start of the start of the experiment). The regions of high σ_f represent attracting lines within the flow.

The tracer advection process was also used to identify the original position of each tracer when the experiment began. The tracers were advected backwards in time from each time step until $t = 0$, and their original height $y_o\left(\mathbf{x}, t\right)$ was identified. The $y_o\left(\mathbf{x}, t\right)$ fields are henceforth referred to simply as the 'tracer fields'. As will be seen, this approach is particularly useful when examining the entrainment process and the composition of the plume throughout its development.

3. Experimental Results

3.1. The Vortex Ring Bubble

It is often useful in studies of convecting vortex rings to examine the flow in a reference frame that is moving with the ring (Dabiri and Gharib, 2004; Shariff and Leonard, 1992). In the current study, this corresponds to a reference frame rising with the plume, and requires an estimate of the plume's rise velocity, which in turn requires an estimate of the plume height

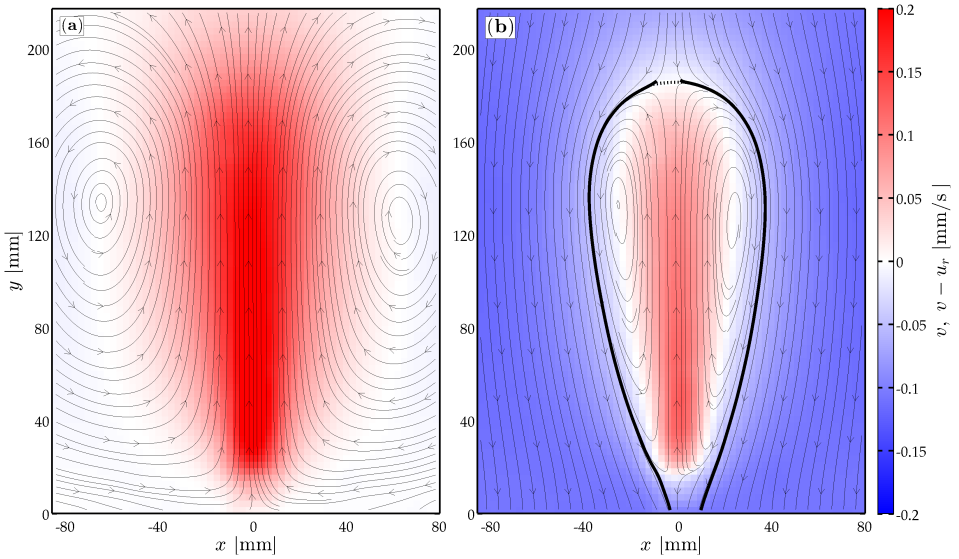

Figure 2: Contours of the vertical velocity and streamlines at $t = 1797$ s and $Ra = 1.36 \times 10^6$, computed in an Eulerian reference frame (a) and one moving with the plume (b). The thick black line in (b) represents the vortex ring bubble.

as a function of time, $y_p(t)$. We derive the plume height from the tracer fields; y_p is defined as the highest point at which the local tracers originated from below the PIV domain ($y \leq 1.39$ mm). This was found to be consistent with the definitions based on the maxima of σ_f (Cagney et al., 2015) and the gradient of the radial velocity (Davaille et al., 2011), but contained less scatter. The rise velocity signal, $u_r(t)$, was then found by differentiating $y_p(t)$ using the least-squares method.

Figure 2(a) shows the vertical component of a sample velocity field with streamlines for the $Ra = 1.36 \times 10^6$ experiment. The streamlines were computed in an Eulerian or 'lab-based' reference frame (i.e. one which is fixed

in space and does not move with the plume), and do not provide a clear indication of the position or geometry of the plume. Two centres of rotation are apparent at $y \approx 130$ mm, as the material is rising along the central axis and induces a return flow near the edges of the PIV domain.

The velocity field can be converted into a reference frame moving with the plume by subtracting $u_r(t)$ from the vertical velocity component, as shown in Figure 2(b). In this case the plume structure is apparent in the streamlines, and has a clear inverted teardrop shape. The heights of the centres of rotation have not changed, but they are now contained within the plume structure. A similar analysis was presented by Davaille et al. (2011).

This figure bears strong similarities to the two-dimensional measurements of a convecting vortex ring presented in Dabiri and Gharib (2004). Now that the velocity fields are in a frame moving with the plume, the vortex ring bubble can be used to define the plume geometry, as shown by the thick black lines enclosing the centres of rotation in Figure 2(b). In order to find these lines, streamlines were computed, starting from the top of the PIV domain with an initial spacing equal to that of the PIV measurement (i.e. $\Delta x = 2.79$ mm). The neighbouring streamlines which moved to either side of the plume axis were identified and the lines were joined at the top of the plume using a spline curve, which is indicated by the thick dashed line in Figure 2(b), to form the VRB.

The VRB is shown at three instances in Figures 3(a-c), overlaid on the tracer fields. The colour denotes the height of each tracer at the time when the heater was turned on, y_o. In each case, the VRB is taken to mark the boundary between the ambient fluid and material in the plume head which

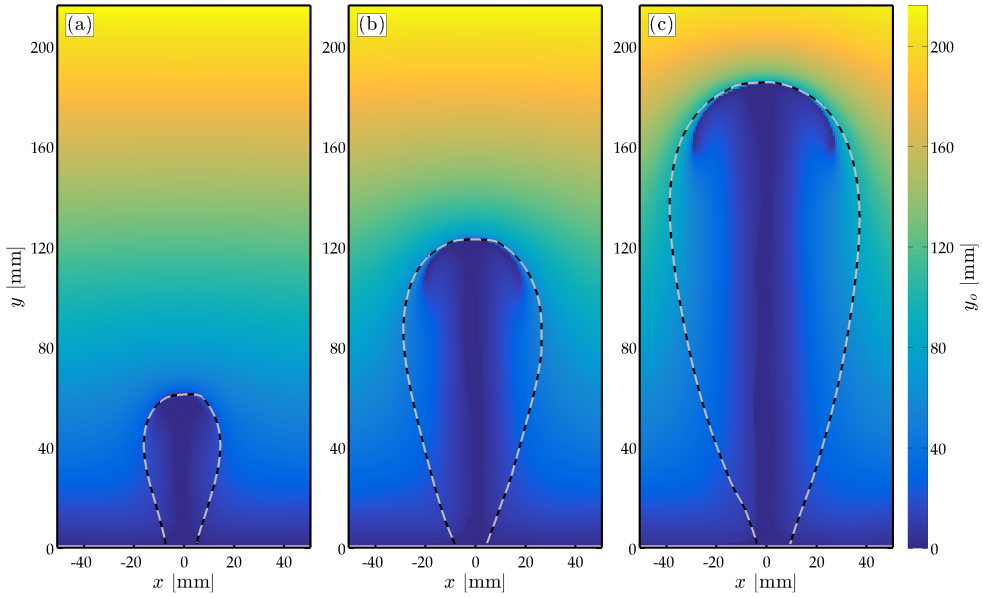

Figure 3: Tracer fields showing the vertical origin of material at $y_p = 60.8$ mm (a), 122.1 mm (b), and 185.2 mm (c), for $Ra = 1.36 \times 10^6$. The vortex ring bubble is shown by the back and white dashed lines, and aligns with the boundary between ambient fluid and that derived from very deep in the fluid domain.

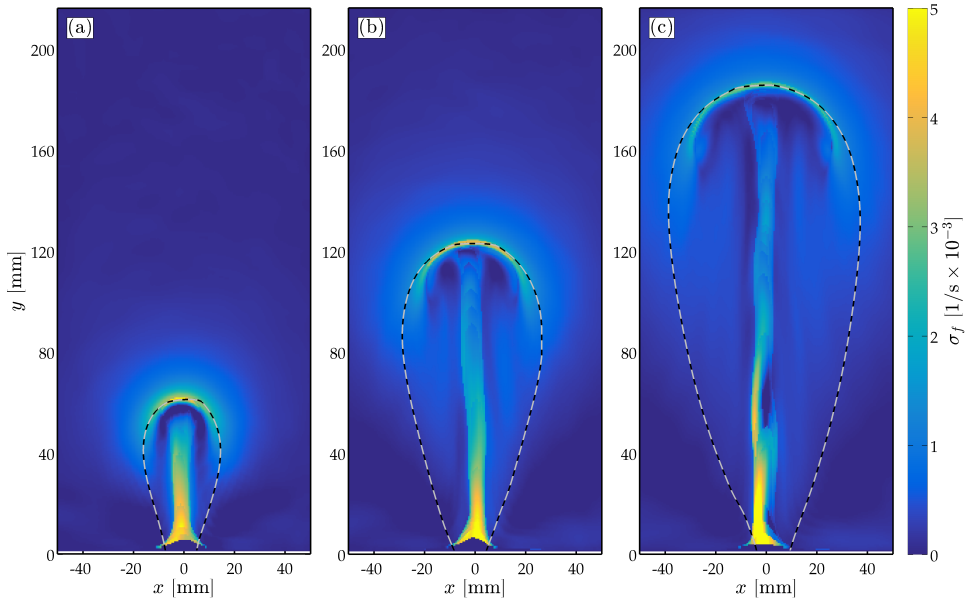

Figure 4: Finite-Time Lyapunov Exponent fields computed at $y_p = 60.8$ mm (a), 122.1 mm (b), and 185.2 mm (c), for $Ra = 1.36 \times 10^6$. The vortex ring bubble is shown by the black and white dashed lines, and aligns with ridge at the top of the plume head.

has risen from deep in the fluid domain. The majority of the fluid contained in the VRB has originated from very deep in the test-section (dark blue regions). This material forms a circular shape at the top of the plume head which closely matches the shape of the VRB in this region.

The VRB is compared to the FTLE fields in Figure 4. The variation in the FTLE fields throughout the growth and rise of a thermal plume is described in detail elsewhere (Cagney et al., 2015), and the current discussion focuses on its relation to the VRB. Ridges in the FTLE tend to separate qualitatively distinct regions of the flow; therefore, any definition of the structures within a flow is required to be consistent with the estimated FTLE fields.

The top of the plume head is marked by a circular arc of high σ_f which represents a Lagrangian Coherent Structure, and aligns closely with the top boundary of the plume. This provides further confidence that the VRB is faithfully identifying the plume geometry. It also indicates that the region at the upper edge of the VRB is characterised by strong fluid stretching and is an attracting line in the flow. A region of high σ_f is also present along the plume axis ($x = 0$), particularly close to the heater. However, this is internal to the plume and does not relate to the VRB.

In general, the definition of the plume geometry is consistent with the tracers and FTLE fields which were calculated independently, providing further evidence that the VRB is an effective means to define the plume geometry.

3.2. Plume Composition and Entrainment

The composition of the plume can also be examined throughout its development using the tracer fields shown in Figure 3. In order to quantify the contribution of tracers originating from different depths in the fluid domain, the tracers contained within the VRB were identified, and histograms were computed of their origin height. The histograms contain 30 bins, spaced equally over the range $y = 0$ to $y_p(t)$. For ease of comparison, the data are presented as a line graph, rather than a bar chart, and the counts for each bin, c_i, are presented in normalised form as a probability distribution:

$$\phi_i' = \frac{c_i}{\sum_i c_i}, \tag{5}$$

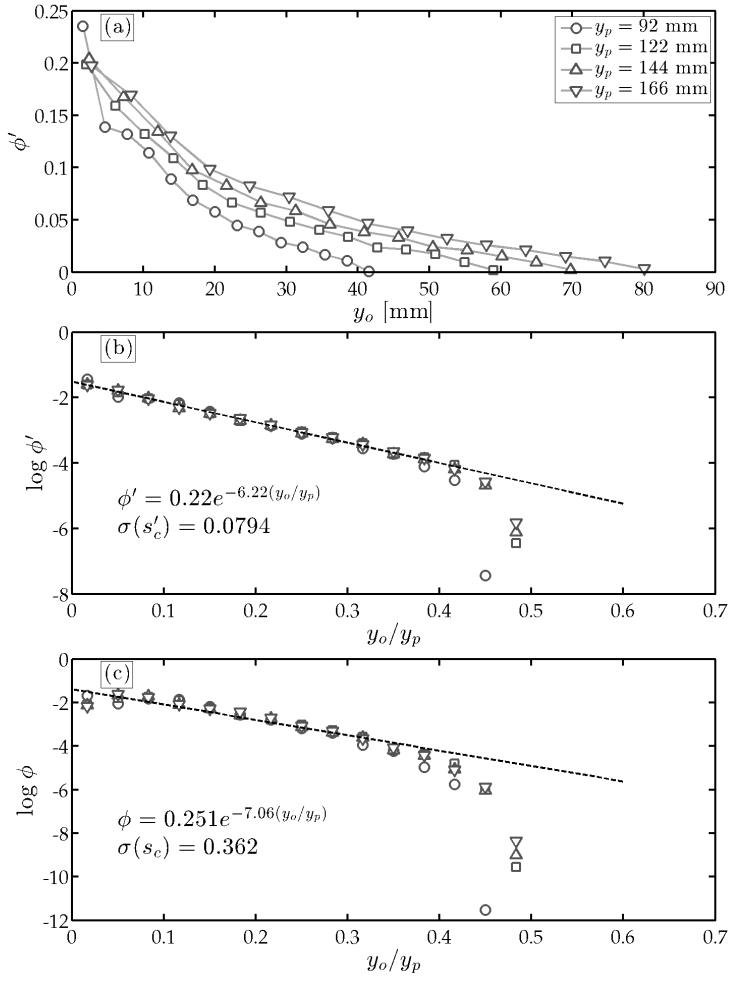

Figure 5: Variation in the composition of the plume for four different plume heights for $Ra = 1.36 \times 10^6$ (a); ϕ' is the normalised number of tracers which originated from a given height, y_o. The exponential distribution of tracers is clear in (b), in which the height of the tracer origin is normalised by the plume height. The three-dimensional distribution, which accounts for the radial position of tracers (Equation 12), is shown in (c).

where $'$ denotes a sectional property (because ϕ_i' and c_i are computed from tracers found in the measurement plane rather than from the entire three-dimensional fields). The distributions all appear to follow an exponential distribution. This is confirmed in Figure 5(b), in which the tracer heights are normalised by the plume height. In this case, all the distributions align closely, and can be described as:

$$\phi' = A' e^{-s_c' y_o / y_p}, \tag{6}$$

where A' and s_c' are non-dimensional constants. These values were found by performing a least-squares fit to the data in Figure 5(b) in the range $0 \leq y_o/y_p < 0.35$, which gave values of $A' = 0.22$ and $s_c' = 6.22$. The r^2 value was 0.991, and the standard deviation of the linear regression was $\sigma(s_c') = 0.093$. The constant s_c' is henceforth referred to as the 'sampling coefficient'.

Equations 5 and 6 relate to two-dimensional plumes, such as those generated in two-dimensional simulations. However, plumes in experiments and the mantle are three-dimensional, and this will affect the tracer distribution and the calculations of the sampling coefficient. This effect can be accounted for by weighting each point in the tracer field in proportion to the volume it occupies in a three-dimensional, axisymmetric space:

$$w_k = \pi(\Delta x_o)^2 |x_k|, \tag{7}$$

where w_k is the weighting factor, Δx_o is the resolution of the tracer fields and $|x_k|$ is the distance of each tracer from the plume axis. The probability distribution (Equation 5) can be modified to account for this:

$$\phi_i = \frac{\sum_{k=1}^{c_i} w_k}{\sum_i \left(\sum_{k=1}^{c_i} w_k \right)}, \tag{8}$$

$$= \frac{\sum_{k=1}^{c_i} |x_k|}{\sum_i \sum_{k=1}^{c_i} |x_k|}. \tag{9}$$

The three-dimensional probability distribution, ϕ (now without a prime, as it is no longer a sectional property), also follows an exponential relationship, as can be seen in Figure 5(c). The gradient is steeper in the three-dimensional case, i.e. $s_c > s'_c$.

For the four plume heights examined, no tracers are identified which had originated from above approximately half the plume height, $y_o/y_p \gtrsim 0.5$. For example, when $y_p = 166$ mm, no tracers were found for $y_o \gtrsim 82$ mm. This is likely to be a consequence of the fact that the top of the plume head is a material line in the flow (indicated by the arc-like ridge in the σ_f fields in Figure 4, Cagney et al. (2015)) and no fluid passes through it, i.e. material does not enter the plume directly from above. In theory the plume will grow by thermal diffusion, and thus may incorporate some material into the head in this manner; however, given the large Pr, this effect is likely to be very small, and negligible in the mantle, where $Pr \sim 10^{22}$.

The parameter A' is dependent on the number of bins used to calculated the histograms. Because no tracers are entrained for $y_p/y_o \gtrsim 0.5$, the integral of the probability distribution can be written as

$$\int_0^{0.5} \phi \ \mathrm{d}\left(\frac{y_o}{y_p}\right) = -\frac{A}{s_c}\left(e^{-s_c/2} - 1\right) = 1, \tag{10}$$

which can be re-arranged to express A as a function of s_c:

$$A = \frac{s_c}{(1 - e^{-s_c/2})}. \tag{11}$$

Therefore, the composition of the material in the VRB can be expressed using only the sampling coefficient,

$$\phi = \frac{s_c}{(1 - e^{-s_c/2})} e^{-s_c y_o/y_p}. \tag{12}$$

The sampling coefficient controls the degree to which the plume samples material from different heights. High-s_c plumes are composed of material originating almost exclusively from very deep in the fluid, while low-s_c plumes entrain a greater proportion of material from different heights. Therefore, the inverse of the sampling coefficient is indicative of the degree of entrainment within a plume. Table 1 summarises the sectional and three-dimensional sampling coefficients found for each of the four experiments. It is apparent that the sampling coefficient is dependent on the Rayleigh number and the viscosity contrast. However, as the two properties are both changing, it is not possible to discern the effect of either variable independently.

The sampling coefficient appears to be independent of time and plume height (Figure 5(b-c)) and Equation 12 does not contain a time-dependency (other than that implicitly contained in $y_p(t)$). This suggests that the entrainment process and the form of the plume can be described by a similarity solution. This feature of the plume growth is demonstrated in Figure 6, which

Ra	γ	s'_c	s_c
0.62×10^6	15.1	5.71	6
0.86×10^6	35.7	5.8	6.06
1.12×10^6	75.9	6.03	6.76
1.36×10^6	141.4	6.22	7.06

Table 1: Summary of the sectional and three-dimensional sampling coefficients found for each of the four experiments.

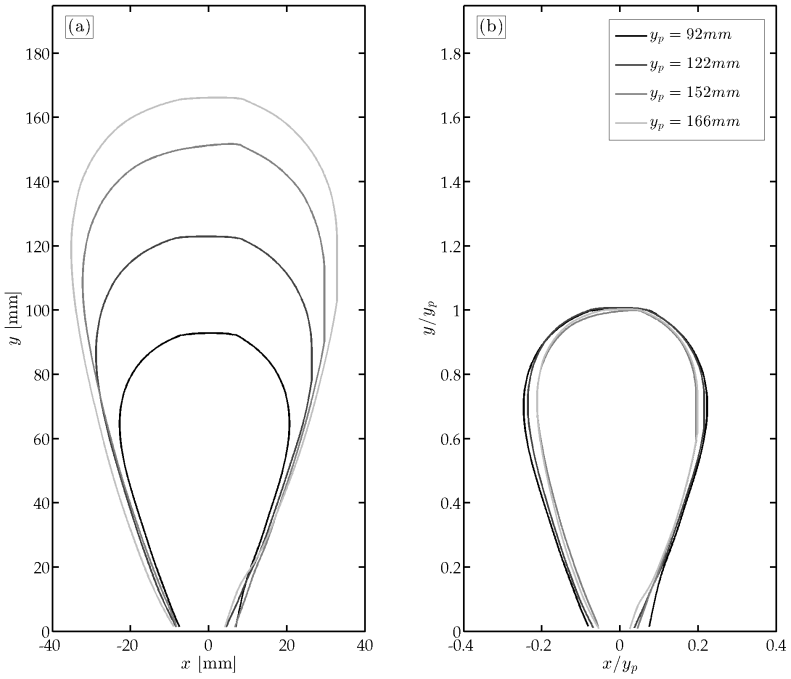

Figure 6: Geometry of the vortex ring bubble calculated at plume heights for $Ra = 1.36 \times 10^6$ (a), and the same geometries normalised by the plume height (b).

shows the VRB calculated at four times and plume heights. When the dimensions are normalised by $y_p(t)$, the four bubbles collapse (Figure 6(b)), indicating that the non-dimensional geometry of the plume and its general shape do not vary with time.

Previous researchers have proposed similarity solutions to describe the steady-state stems of laminar and turbulent plumes (Batchelor, 1954; Hauri et al., 1994) and isolated thermals (Griffiths, 1991; Whittaker and Lister, 2008; Peng and Lister, 2014). The current work empirically shows that this condition is also applicable to the entire plume, and indicates that this may be a fruitful approach for future analytical work.

4. Application to the mantle

4.1. Numerical Details

The data presented in Table 1 shows that the sampling coefficient increases with the applied temperature difference. However, both the Rayleigh number and the viscosity contrast are also varying, and it is difficult to distinguish between the influence of Ra and γ. In order to isolate the effect of both parameters on the plume composition, numerical simulations were performed in which Ra and γ were varied independently.

The simulations were designed to replicate conditions in the test-section. The fluid domain was cubic with dimensions of 265 mm in each direction, and except where otherwise stated, the fluid properties were the same as those of the syrup (Section 2). The fluid was assumed to have an infinite Prandtl number and the Boussinesq approximation was employed. The relevant non-dimensional equations for conservation of mass, momentum and energy are:

$$\vec{\nabla} \cdot \vec{v} = 0 \tag{13}$$

$$\vec{\nabla} \cdot \varsigma_{ij} - \vec{\nabla} p = Ra\Theta\hat{\vec{e}_y} \tag{14}$$

$$\frac{\partial T}{\partial t} = \nabla^2 T - \vec{v} \cdot \vec{\nabla} T \tag{15}$$

where v is the velocity vector, ς_{ij} is the deviatoric stress tensor, p the pressure, Θ the non-dimensional temperature, and $\hat{\vec{e}_y}$ the vertical unit vector. The rheology of the fluid was given by Equation 1.

The model is solely heated by a circular patch at the centre of the lower surface, with the same dimensions and thermal properties as in the laboratory setup. All other boundaries had a rigid no-slip condition, and (except for the constant temperature of the circular heater) were insulating by applying a zero heat flux condition.

Two suites of simulations were performed; one in which the viscosity contrast was fixed at $\gamma = 141.4$ and the Rayleigh number varied (the Ra-suite) and one in which the Rayleigh number was held constant at 1.36×10^6 and the viscosity contrast was varied (the γ-suite). For the former suite, the Rayleigh number was varied in the range $Ra = 10^5 - 10^8$ by varying the fluid density, while in the latter suite the viscosity contrast was controlled by varying ΔT for the range $\gamma = 2 - 490$, and κ was altered to ensure that Ra remained constant. An additional iso-viscous case was examined, in which the viscosity throughout the fluid was set to the ambient value.

Calculations were performed in three-dimensional Cartesian geometry with a standard resolution of $128 \times 128 \times 128$ ($n_x \times n_y \times n_z$) grid points

and 100 Lagrangian tracers per cell has been tested and is applied. For the Ra-suite, a higher resolution (i.e., $256 \times 256 \times 256$) was required to ensure a suitable representation of the increasingly thin boundary layer with higher Ra-numbers. The physical model described above was solved by the finite-difference/volume multigrid code StagYY (Tackley, 2008), and the high resolution experiments are run on the UK's National High Performance Computing Facility ARCHER.

In order to analyse the numerical results and compare to the experimental data, the velocity field from the centre plane of the plume was extracted (i.e. the same plane that was measured using PIV in the experiments).

4.2. Sampling Coefficient in the Mantle

The results of the numerical simulations were first compared to the experimental data in order to confirm that they were adequately capturing the flow physics. Figures 7(a) and 7(b) show the tracer fields calculated from the experimental and numerical results, respectively, for $y_p = 130$ mm and $Ra = 1.36 \times 10^6$. The similarity between the two fields is clear. The scrolls in the plume head are particularly noticeable in the numerical data, which may be a result of the infinite-Pr assumption; in the experimental case, thermal diffusion ensures that the temperature gradients and viscosity contrast are small outside the vicinity of the heater. However, in the numerical case the role of thermal diffusion is weak, and larger temperature gradients and viscosity contrasts can be sustained and the tracer fields can have a much finer structure (in this case, well-defined scrolls in the plume head).

Profiles of the vertical velocity for both cases are shown in Figures 7(c) and 7(d) for $y = y_p/3$ and $y = 2y_p/3$, respectively. The numerical and exper-

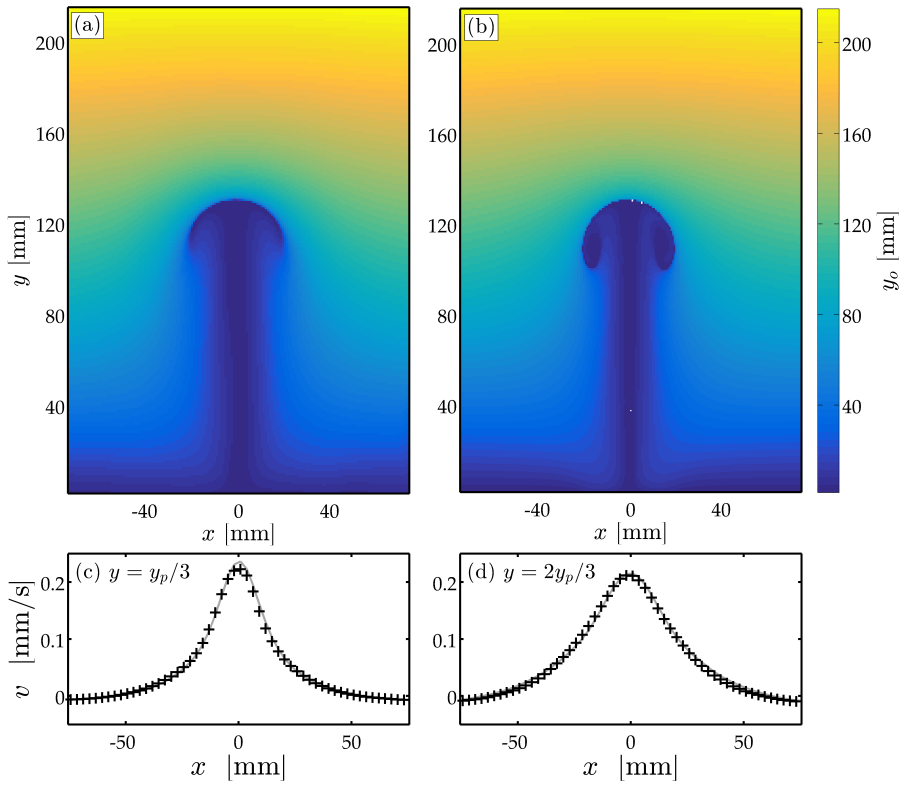

Figure 7: Tracer fields computed from the experimental (a) and numerical (b) data, for $Ra = 1.36 \times 10^6$, $\gamma = 141.4$ and $y_p = 130$ mm. Profiles of the vertical velocity for the same times are shown in (c) at $y = y_p/3$, and (d) at $y = 2y_p/3$; experimental data (black crosses), numerical data (grey lines).

imental profiles align very closely. Along with the strong similarity between the tracer fields, Figure 7 indicates that the simulations are successfully replicating the flow occurring in the experiments and can be used to predict the plume dynamics.

The dependence of s_c on Ra and γ is shown in Figure 8. The error bars are given by the standard deviation found from the linear regression performed between each set of $\log\phi_i$ and y_i/y_p. The sampling coefficient has a log-linear relationship with Rayleigh number (Figure 8(a)). The trend line suggests that s_c becomes negative for $Ra \lesssim 10^{4.5}$, which is physically unrealistic (corresponding to a plume which contains very little material from deep in the domain but is primarily composed of fluid from $y \approx y_p/2$). Therefore, the log-linear relationship is likely to breakdown at some point for $Ra < 10^5$, although such values are not relevant to mantle convection. The sampling coefficient increases with Ra, implying that the more vigorous the convection, the greater the proportion of plume material is derived from near the thermal boundary layer at which the plumes formed (most likely the core-mantle boundary, but potentially also the transition zone).

A log-linear relationship also exists between the sampling coefficient and the viscosity contrast (Figure 8(b)). The trend lines indicate that Ra and γ have opposite effects on the entrainment process; increasing the viscosity contrast *decreases* the proportion of plume material derived from deep in the fluid domain.

Using a two-dimensional best-fit, the sampling coefficient can be expressed as

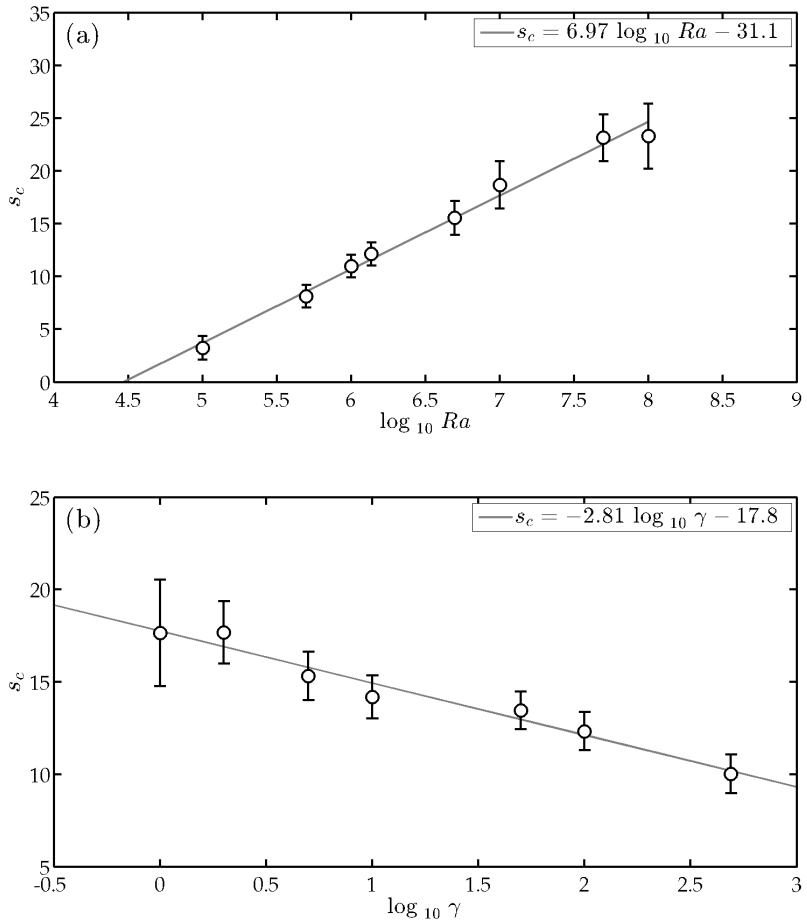

Figure 8: Variation in the predicted sampling coefficient of plumes as a function of Rayleigh number at $\gamma = 141.4$ (a), and as a function of viscosity contrast at $Ra = 1.36 \times 10^6$ (b). The grey lines represent the best-fit linear trend between s_c and the log values.

$$s_c = 6.97 \log_{10} Ra - 2.83 \log_{10} \gamma - 24.98. \quad (16)$$

The magnitude of the $\log_{10} Ra$ term is greater than that of the $\log_{10} \gamma$ term, indicating that the Rayleigh number plays a greater role in determining the composition of mantle plumes.

The values of the Rayleigh number and viscosity contrast in the mantle are poorly constrained, due to a combination of uncertainties in the various physical properties of mantle material and their dependence on depth and chemical heterogeneity. Estimates of the Rayleigh number are typically in the range $10^6 - 10^8$, while the viscosity contrast is likely to be somewhere between 100 and 1000. In this case, Equation 16 predicts that a plume in the mantle will have a sampling coefficient in the range 8.3 - 25.1.

To put this into physical terms regarding the plume composition, it is useful to consider the integral of ϕ,

$$\Phi = \int_0^{y_o/y_p} \phi \ \mathrm{d}\left(\frac{y_o}{y_p}\right) = \frac{1 - e^{-s_c y_o/y_p}}{1 - e^{-s_c/2}}. \quad (17)$$

In effect, $\Phi\,(y_o/y_p)$ is equal to the proportion of the plume material which originated from $y \leq y_o$. Figure 9 shows the variation in the proportion of a plume which has been derived from the deepest 10 km in the mantle as the plume rises, for $s_c = 8.3$ and 25.1. In both cases $\Phi_{(y_o=10 \text{ km})}$ decreases exponentially, but the deep mantle component remains greater for the $s_c = 25.1$ case. Figure 9 indicates that as a mantle plume reaches the transition zone, between 3.7 and 10.7% of its material will have originated from the deepest 10 km in the mantle.

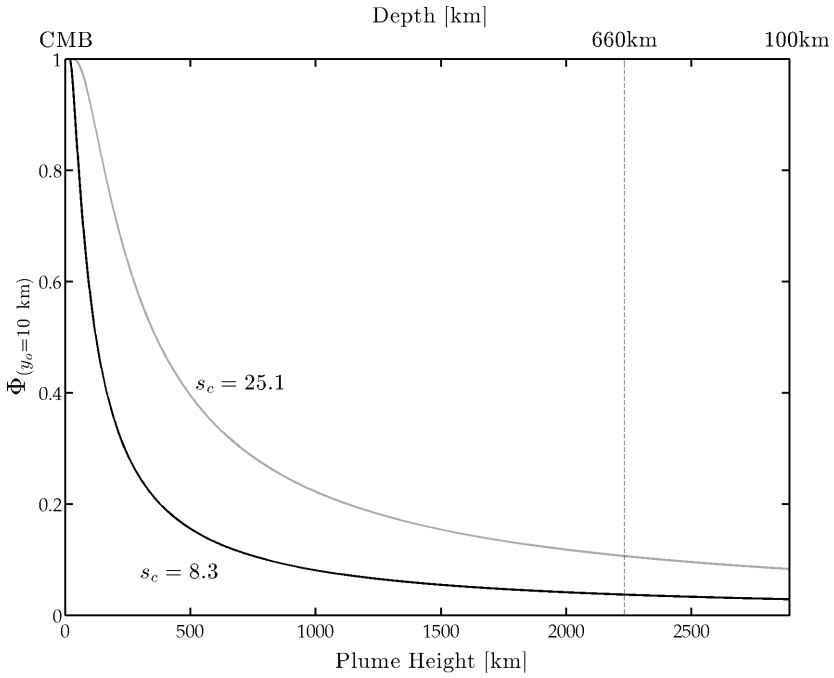

Figure 9: Proportion of a plume derived from the lowermost 10 km in the mantle as a function of plume height for two different values of the sampling coefficient.

5. Discussion

The analysis presented in the previous section is relevant to the role of mantle plumes in redistributing siderophilic elements throughout the mantle. There is conflicting evidence as to whether plumes contain material from the core, as suggested by the Osmium signatures found in some hot spot basalts and LIPs (Hawkesworth and Scherstén, 2007; Walker et al., 1995; White, 2010). The lowermost region of the mantle, close to the core-mantle boundary, is likely to contain elevated traces of siderophilic elements relative to the rest of the mantle; Equation 17 describes how siderophilic elements near the CMB will be distributed throughout the mantle over time.

These results also have very significant implications for the geochemical interpretation of hot spot basalts. As our study examines a rising plume, rather than the plume tail after the head has reached the surface, our results are particularly relevant to the interpretations of LIPs. The exact composition of hot spot basalts will not be the same as the composition of a rising plume (i.e. as described by the sampling coefficient and Equation 17) (Ballmer et al., 2011); however, as conduction plays a negligible role in mantle dynamics on the time scale of a rising plume, the material outside the plume is unlikely to experience significant melting and Equation 17 therefore represents a *constraint on the source of OIBs*. Plumes may experience some entrainment as they interact with major phase transitions or the lithosphere and their dynamics become too complex to be described by a simple analytical equation, although these contributions to the geochemical signatures of basalts are thought to be small (Farnetani and Richards, 1995; Farnetani et al., 2002). The results presented here show that the material in OIBs is

primarily derived from very deep in the mantle (most likely the lowermost few hundred kilometres).

This supports the geochemical study of Hart et al. (1992), who argued that OIBs are derived from the lower mantle, and contain little or no material derived from the mid- or upper-mantle. Our analysis provides a framework to explain these geochemical observations, and also quantifies the *degree* to which mantle plumes are derived from the lower mantle; by the time a plume is within 10 km of the surface, Equation 17 indicates that 90% of the plume material has been derived from the lowermost $260 - 750$ km in the mantle (depending on the value of s_c).

These findings also have important implications for isotope geochemistry, and what it may tell us about the chemical composition of the mantle. The results presented here imply that the geochemical signature of OIBs is derived from the deeper half of the lower mantle, with some likely contribution from regions near the major phase transitions and lithosphere; therefore the various known geochemical reservoirs must exist in one or more of these regions. These reservoirs include the Enriched Mantle (derived from subducted slabs) and FOZO end-members, as well as the high $^3He/^4He$ regions of 'primitive' mantle (Hofmann, 1997; Hart et al., 1992; van Keken et al., 2002).

Perhaps more significantly, it implies that the shallower half of the lower mantle will have a very small or negligible contribution to mantle plumes and will effectively be invisible in OIBs, and isotope geochemistry cannot be used to make any direct inference about this region. Therefore, various models of mantle heterogeneity that include large-scale reservoirs of primitive mantle material in this region (see reviews by Tackley (2000) and van Keken et al.

(2002)) cannot be tested using isotope geochemistry alone.

Future work is planned to investigate what effect features such as stress- and pressure-dependent rheology and phase transitions may have on the plume composition and the implications for geochemistry discussed here.

Conclusions

In this study, we used our laboratory model to examine thermal plumes rising through a viscous syrup and provided a empirical measure to constrain the source region of mantle plumes. The velocity fields were measured using Stereoscopic Particle-Image Velocimetry.

Following the work of Turner (1957), plumes were treated as a special case of vortex rings, and the concept of the 'vortex ring bubble' was used to provide the first objective definition of a plume's geometry. This definition was shown to be consistent with the Finite-Time Lyapunov Exponents and tracer fields. This novel description of the plume geometry allows the source region of a plume to be quantified in terms of depth; material in the plume primarily originated from deep in the fluid domain, and the distribution of the material was found to follow a clear exponential relationship that depends on a single variable, the sampling coefficient, s_c. The distribution does not have an explicit dependency on time, and our results show that the plume geometry is self-similar, in support of previous analytical work.

Additionally, numerical simulations were performed in which the Rayleigh number and viscosity contrast were varied independently in order to isolate their effect on the plume's source region. The simulation results were in good agreement to the experimental data, and showed that the sampling

coefficient has a log-linear relationship with both the Rayleigh number and viscosity contrast. The Rayleigh number has a strong effect on the sampling coefficient, implying that the more vigorous the convection in the mantle, the greater proportion of plume material will be derived from close to the core-mantle boundary. From the numerical results, we predicted that plumes in the mantle have a coefficient in the range $s_c = 8.3 - 25.1$, which allowed us to constrain the source of hot spot basalts. This crucially indicates that the vast majority of plume material derives from the deep mantle, in agreement with previous geochemical studies (Hart et al., 1992; Walker et al., 1995). Furthermore, it showed that isotope geochemistry studies of hot spots basalts will provide little information on regions above approximately 1000 km from the CMB, and that the various known geochemical reservoirs must lie within a few hundred kilometres of the CMB.

6. Acknowledgements

We would like to thank Maxim Ballmer and another anonymous reviewer for their constructive comments and suggestions. This work was funded by the National Science Foundation (grant EAR-055199), the MAPS Dean's Office at UCL and the CIDER workshop (EAR-1135452). The computational work presented here was computed using the UK National High Performance Computing Facility (ARCHER).

References

Ballmer, M. D., Ito, G., van Hunen, J., Tackley, P. J., 2011. Spatial and temporal variability in Hawaiian hotspot volcanism induced by small-scale

convection. Nature Geoscience 4, 457 – 460.

Batchelor, G. K., 1954. Heat convection and buoyancy effects in fluids. Quarterly Journal of the Royal Meteorological Society 80, 339–354.

Bianco, T. A., Ito, G., van Hunen, J., Ballmer, M. D., Mahoney, J. J., 2008. Geochemical variation at the Hawaiian hot spot caused by upper mantle dynamics and melting of a heterogeneous plume. Geochemistry, Geophysics, Geosystems 9 (11), Q11003.

Cagney, N., Newsome, W. H., Lithgow-Bertelloni, C., Cotel, A., Hart, S. R., Whitehead, J. A., 2015. Temperature and velocity measurements of a rising thermal plume. Geochemistry, Geophysics, Geosystems 16, 1–21.

Campbell, I. H., 2005. Large igneous provinces and the mantle plume hypothesis. Elements 1, 265–269.

Chay, A., Schlien, D. J., 1986. Scalar field measurements of a laminar starting plume cap using digital processing of interferograms. Physics of Fluids 29, 2358–2366.

Dabiri, J. O., Gharib, M., 2004. Fluid entrainment by isolated vortex rings. Journal of Fluid Mechanics 511, 311–331.

Davaille, A., Limare, A., Touitou, F., Kumagai, I., Vatteville, J., 2011. Anatomy of a laminar starting thermal plume at high Prandtl number. Experiments in Fluids 50, 285–300.

Farnetani, C. G., Legras, E., Tackley, P. J., 2002. Mixing and deformations in mantle plumes. Earth and Planetary Science Letters 196, 1–15.

Farnetani, C. G., Richards, M. A., 1995. Thermal entrainment and melting in mantle plumes. Earth and Planetary Science Letters, 251–267.

Griffiths, R. W., 1986. Thermals in extremely viscous fluids, including the effects of temperature-dependent viscosity. Journal of Fluid Mechanics 166, 115–138.

Griffiths, R. W., 1991. Entrainment and stirring in viscous plumes. Physics of Fluids A 3 (5), 1233–1242.

Griffiths, R. W., Campbell, I. H., 1990. Stirring and structure in mantle starting plumes. Earth and Planetary Science Letters 99, 66–78.

Haller, G., 2015. Lagrangian coherent structures. Annual Review of Fluid Mechanics 47, 137–161.

Hart, S. R., Hauri, E. H., Oschmann, L. A., Whitehead, J. A., 1992. Mantle plumes and entrainment: isotopic evidence. Science 256, 517–520.

Hauri, E. H., Whitehead, J. A., Hart, S. R., 1994. Fluid dynamic and geochemical aspects of entrainment in mantle plumes. Journal of Geophysical Research 99 (B12), 24275–24300.

Hawkesworth, C., Scherstén, A., 2007. Mantle plumes and geochemistry. Chemical Geology 241, 319–331.

Hofmann, A. W., 1997. Mantle geochemistry: the message from oceanic volcanism. Nature 385 (16), 219–229.

Hofmann, A. W., Farnetani, C. G., 2013. Two views of the Hawaiian plume structure. Geochemistry, Geophysics, Geosystems 14, 5308–5322.

Kellogg, L. H., 1992. Mixing in the mantle. Annual Review of Earth and Planetary Sciences 20, 365–388.

Lin, S.-C., van Keken, P. E., 2006. Deformation, stirring and material transport in thermochemical plumes. Geophysical Research Letters 33 (L20306).

Morgan, W. J., 1971. Convective plumes in the lower mantle. Nature 230, 42–43.

Peng, G. G., Lister, J. R., 2014. The initial transient and approach to self-similarity of a very viscous buoyant thermal. Journal of Fluid Mechanics 744, 352–375.

Pottebaum, T. S., Gharib, M., 2004. The pinch-off process in a starting buoyant plume. Experiments in Fluids 37, 87–94.

Richards, M. A., Duncan, R. A., Courtillot, V. E., 1989. Flood basalts and hot-spot tracks: plume heads and tails. Science 246 (4926), 103–107.

Schlien, D. J., 1976. Some laminar thermal and plume experiments. Physics of Fluids 19 (8), 1089–1098.

Shariff, K., Leonard, A., 1992. Vortex rings. Annual Review of Fluid Mechanics 24, 235–279.

Shusser, M., Gharib, M., 2000. A model for vortex ring formation in a starting buoyant plume. Journal of Fluid Mechanics 416, 173–185.

Tackley, P. J., June 2000. Mantle convection and plate tectonics: Toward an integrated physical and chemical theory. Science 288 (5473), 2002–2007.

Tackley, P. J., 2008. Modelling compressible mantle convection with large viscosity contrasts in a three-dimensional spherical shell using the yin-yang grid. Physics of the Earth and Planetary Interiors 171 (1-4), 7–18.

Turner, J. S., 1957. Buoyant vortex rings. Proceedings of the Royal Society of London A, Mathematical and Physical Sciences 239 (1216), 61–75.

van Keken, P. E., Hauri, E. H., Ballentine, C. J., 2002. Mantle mixing: The generation, preservation, and destruction of chemical heterogeneity. Annual Review of Earth and Planetary Sciences 30, 493–525.

Walker, R. J., Morgan, J. W., Horan, M. F., 1995. Osmium-187 enrichment in some plumes: Evidence for core-mantle interaction. Science 260, 819–822.

White, W. M., 2010. Oceanic island basalts and mantle plumes: The geochemical perspective. Annual Review of Earth and Planetary Sciences 38, 133–160.

Whitehead, J. A., Cotel, A., Hart, S., Lithgow-Bertelloni, Newsome, W., 2013. Numerical calculations of two-dimensional large Prandtl number convection in a box. Journal of Fluid Mechanics 729, 584–602.

Whittaker, R. J., Lister, J. R., 2008. The self-similar rise of a buoyant thermal in very viscous flow. Journal of Fluid Mechanics 606, 295–324.